HHS Public Access

Author manuscript

ACS Nano. Author manuscript; available in PMC 2016 December 29.

Published in final edited form as:

ACS Nano. 2016 November 22; 10(11): 9927–9937. doi:10.1021/acsnano.6b03835.

In Vitro and *in Vivo* Mechanism of Bone Tumor Inhibition by Selenium-Doped Bone Mineral Nanoparticles

Yifan Wang[†,‡,○], **Jianglin Wang**[†,§,○], **Hang Hao**[†,‡], **Mingle Cai**[†,‡], **Shiyao Wang**[†,‡], **Jun Ma**[†,‡], **Yan Li**[‖], **Chuanbin Mao**[§,⊥,*], and **Shengmin Zhang**[†,‡,*]

[†]Advanced Biomaterials and Tissue Engineering Center, Huazhong University of Science and Technology, Wuhan 430074, China

[‡]Department of Biomedical Engineering, Huazhong University of Science and Technology, Wuhan 430074, China

[§]Department of Chemistry and Biochemistry, Stephenson Life Sciences Research Center, University of Oklahoma, Norman, Oklahoma 73019, United States

[‖]Department of Oncology, Hubei Key Laboratory of Tumor Biological Behaviors and Hubei Cancer Clinical Study Center, Zhongnan Hospital of Wuhan University, Wuhan 430071, China

[⊥]School of Materials Science and Engineering, Zhejiang University, Hangzhou, Zhejiang 310027, China

Abstract

Biocompatible tissue-borne crystalline nanoparticles releasing anticancer therapeutic inorganic elements are intriguing therapeutics holding the promise for both tissue repair and cancer therapy. However, how the therapeutic inorganic elements released from the lattice of such nanoparticles induce tumor inhibition remains unclear. Here we use selenium-doped hydroxyapatite nanoparticles (Se-HANs), which could potentially fill the bone defect generated from bone tumor removal while killing residual tumor cells, as an example to study the mechanism by which selenium released from the lattice of Se-HANs induces apoptosis of bone cancer cells *in vitro* and inhibits the growth of bone tumors *in vivo*. We found that Se-HANs induced apoptosis of tumor cells by an inherent caspase-dependent apoptosis pathway synergistically orchestrated with the generation of reactive oxygen species. Such mechanism was further validated by *in vivo* animal evaluation in which Se-HANs tremendously induced tumor apoptosis to inhibit tumor growth while reducing systemic toxicity. Our work proposes a feasible paradigm toward the design of

[*]**Corresponding Authors**. cbmao@ou.edu. smzhang@mail.hust.edu.cn.

[○]These authors contributed equally.

ASSOCIATED CONTENT

Supporting Information

The Supporting Information is available free of charge on the ACS Publications website at DOI: 10.1021/acsnano.6b03835.

Average particle size, zeta potential, and degradation kinetics of nanoparticles; tumor volume curves, nude mice body weight; normal BALB/c mice body weight, blood biochemical analysis, visceral index, histological analysis of liver tissues, and experimental section of the Se-HANs systemic toxicity evaluation (PDF)

The authors declare no competing financial interest.

tissue-repairing inorganic nanoparticles that bear therapeutic ions in the lattice and can release them *in vivo* for inhibiting tumor formation.

Graphical abstract

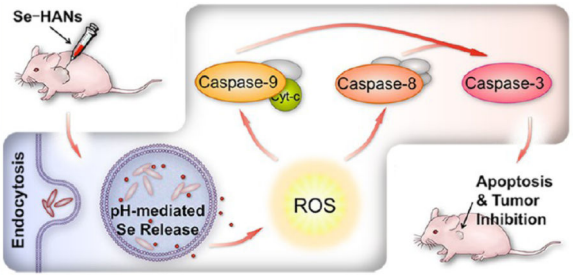

Keywords

tumor inhibition; apoptosis; selenium; nanoparticles; osteosarcoma

Bone cancer is one of the most prevalent cancers with the lowest long-term survival rate among children and adolescents.[1] The most common type of bone cancer is osteosarcoma. Osteosarcoma is a primary malignant solid tumor of bone-forming stem cell origin. It often germinates in the distal femur and proximal tibia and easily metastasizes to lungs.[2,3] Current clinical treatment of osteosarcoma, such as directed resection, can remove the tumor lesions. However, residual tumor cells still remain in the periphery of the bone defect site. Adjuvant chemotherapy is accordingly indispensable for killing the residual tumor cells and preventing tumor recurrence. Meanwhile, to ease the physical limitation of patients, the defect generated by an operation also needs to be filled for bone repair.[4] Biocompatible bone mineral nanoparticles releasing anticancer chemotherapeutic agents are of great potential for satisfying both of the above requirements at the same time.

Since traditional chemotherapy drugs are prone to cause torturous late effects such as anthracycline-induced cardiomyopathy,[5] cisplatin-related renal dysfunction,[6] and hearing loss,[7] nutritional trace elements with antitumor effects, which are also necessary for human health, may be a better choice for the osteosarcoma therapy. To the best of our knowledge, selenium is such an element. We, together with several other groups, have demonstrated that selenium is a crucial anticarcinogen,[8] and selenium deficiency is highly associated with the risk of many health problems[9] and multiple cancers in bone,[10,11] lung,[12] breast,[13] ovarian,[14] prostate,[15,16] and gastrointestin.[17] Up to now, the antitumor function of selenium has been extensively confirmed. Many studies showed that the cytotoxic effect of selenium against several human cancer cell lines was associated with an increase in the level of intracellular reactive oxygen species (ROS).[18,19] However, the exact mechanism involved in tumor suppression by selenium, especially in a form of inorganic ions released from mineral nanoparticles, remains unclear. To gain an understanding of such mechanism, we created an intelligent biomaterial of selenium-doped hydroxyapatite nanoparticles (Se-HANs) with biodegradable and pH-sensitive properties. Meanwhile, Se-HANs could potentially play a dual role in treating osteosarcoma *via* chemotherapy arising from selenium ions and

promoting bone regeneration by hydroxyapatite nanoparticles. In this study, the *in vitro* cellular uptake, degradation and cytotoxicity, the *in vivo* tumor growth inhibition, and systemic toxicity of Se-HANs were extensively evaluated. More importantly, the inherent mechanism of osteosarcoma suppression was systematically investigated (Figure 1).

RESULTS AND DISCUSSION

Selenium Release from the Lattice of the Se-HANs through a pH-Sensitive Degradation Fashion

Natural bone is a hierarchically structured material assembled from basic building blocks of mineral nanoparticles in the frame of bone collagen protein.[20] Hydroxyapatite (HA) is a main inorganic mineral in vertebrate bones and tooth enamels and has been widely studied as excellent bone substitutes.[21] In this work, a series of biodegradable and pH-sensitive Se-HANs including 3%Se-HANs, 6%Se-HANs, and 10%Se-HANs were separately synthesized by a modified aqueous precipitation method based on our former work.[22] Selenium-free HANs and pure sodium selenite (Na_2SeO_3) were designed for controls. X-ray diffraction (XRD) analysis confirmed that the typical peaks of HA were present in all Se-HANs, and there was no significant difference between Se-HANs and the standard HA (JCPDS card no. 09-0432) (Figure 2A). The size, morphology, and colloidal stability in biological solutions are important factors that should be considered in designing nanoparticles.[23] Nanoparticles with a size under 100 nm possess better cell endocytosis efficiency than those with a larger size.[24] HA nanoparticles with needle-like morphology were confirmed to have an ideal mechanical compatibility to natural bone and significantly promote osteogenesis.[25] In this study, dynamic light scattering (DLS) and transmission electron microscopy (TEM) results demonstrated that by using such a modified aqueous precipitation method, the size of needle-like Se-HANs and HANs was controlled within 100 nm. These nanoparticles were also dispersed well in the PBS solution and capable of forming a stable colloid even after stored for over a month (Figure 2B–D and Table S1). Moreover, elemental mapping showed that element distribution of selenium in Se-HANs was similar to that of calcium and phosphorus, indicating that selenium has been completely incorporated into HA lattices and evenly distributed in entire nanoparticles (Figure 2E). These findings imply that the incorporation of selenium ions into HA lattices does not alter the primary features of HANs including physical dimension, geometrical shape, and crystal lattice. The integrated selenium ions have a potential capacity to be delivered *via* a degradation-medicated sustained release, like calcium and phosphate ions.

We proceeded to investigate the release kinetics of Se-HANs in two different PBS buffers of pH 7.4 and pH 5.0. The former was used to simulate the normal healthy tissue, while the latter was designed as a biomimetic acidic microenvironment of tumor tissue.[26] The results showed that the selenium release from Se-HANs was much greater in the acidic condition than in the neutral condition. After release for 12 h in the acidic condition, the accumulation of selenium in 3%Se-HANs, 6%Se-HANs, and 10%Se-HANs reached up to 40.3%, 42.2%, and 54.1%, respectively (Figure 2F). Also, the release rate of selenium was significantly elevated with the increase of selenium content in different compounds. In both acidic and neutral conditions, there was an obvious two-stage release. The first stage (0–24 h) was short

and belonged to a phase of burst release, whereas the second stage (24–120 h) was long and ascribed to a phase of sustained release. Moreover, we found that the release of Ca^{2+} ions was highly associated with the degradation kinetics of as-prepared nanoparticles and was sensitively influenced by pH value, as the nanoparticle degradation was much greater in acid conditions of pH 5.0 than in neutral conditions of pH 7.4 (Figure S1). Therefore, these results clearly indicate that the selenium release from nanoparticles is a typical degradation-mediated pattern, and the current Se-HANs are indeed highly sensitive to environmental pH and can be employed as an effective pH-sensitive nanocarrier.

Degradation of the Internalized Se-HANs Restrains the Viability of Osteosarcoma Cells

We first evaluated the response of Se-HANs to human osteosarcoma cells MNNG/HOS and studied the degradation behavior *in vitro*. The results showed that Se-HANs were able to be readily internalized in osteosarcoma cells *via* nonspecific endocytosis, where they were initially encapsulated in the endosomes and finally transported to the lysosome with the acidic microenvironment for intracellular degradation (Figure 3A,B). We applied fluorescence intensity of FITC-labeled nanoparticles as a quantitative indicator to evaluate intracellular degradation of nanoparticles. We found that the internalized nanoparticles were gradually degraded in the lysosomes to result in a corresponding fluorescent decay with the increase of incubation time, and 10%Se-HANs presented the highest decrease among all nanoparticles (Figure 3C). Moreover, cell viability was highly associated with the degradation of Se-HANs. After cell-nanoparticle interaction for 18 h, cell viabilities of 10%Se-HANs, 6%Se-HANs, 3%Se-HANs, HANs, and Na_2SeO_3 were 17%, 50%, 97%, 100%, and 31%, respectively (Figure 3D). Na_2SeO_3, used as a positive inhibition control, showed an obvious inhibition effect. Its inhibition performance was superior to all the other groups before 12 h, but was inferior to 10%Se-HANs after 18 h. These findings imply that the selenium content in different Se-HANs affects nanoparticle degradation in the lysosome and cell viability. Higher selenium content of Se-HANs generates a faster degradation and thus results in a lower cell viability.

Se-HANs Induce Apoptosis of Tumor Cells through an Inherent Caspase-Dependent Apoptosis Pathway Synergistically Orchestrated with ROS Generation

Many mineral nanoparticles used as antitumor agents have been found to kill tumor cells through ROS induction.[27–30] For instance, Zn^{2+} ions from intracellular dissolution of ZnO nanoparticles could trigger ROS generation,[31] thereby activating a p53-mediated cell death pathway.[32,33] Analogously, in our study, selenium ions were released within osteosarcoma cells through the degradation of Se-HANs and resulted in the decline of cell viability. Recent studies have reported that antitumor activities of selenium ions are probably due to the apoptosis of tumor cells, particularly those mediated by ROS.[34,35] Hence, we surmised that such a low cell viability was probably caused by selenium-induced ROS generation and the subsequent cell apoptosis. To confirm such inference, we monitored a unique indicator of ROS, a fluorescent product of 2′,7-dichlorofluorescein (DCF) generated during the process of ROS formation. The results showed that both 3% Se-HANs and HANs exhibited no detectable DCF, whereas there was a remarkable increase of DCF in the compounds with higher selenium content including 6%Se-HANs, 10%Se-HANs, and 2 μM Na_2 SeO_3 (Figure 3E). Also, we verified that the compounds with a higher selenium content displayed a nearly

100% cell viability throughout the coculture of nanoparticles and cells for 48 h (Figure 3F), as they could not induce osteosarcoma apoptosis after intracellular ROS generation was inhibited by adding MnTMPyP (Figure 3G). Therefore, these data imply that ROS generation plays a pivotal role in the process of selenium-induced tumor apoptosis. This is consistent with the earlier findings that ROS generation could induce osteosarcoma destruction.[34]

It is well documented that caspase-3, as a key apoptotic executioner, can be activated by caspase-8 and caspase-9. Caspase-8 is an apoptotic initiator of the death receptor-mediated extrinsic pathway, whereas caspase-9 is an apoptotic initiator of the mitochondria-mediated intrinsic pathway.[24,36] To prove the possible mechanism of caspases-dependent apoptosis, we successfully detected the activated/cleaved caspase-3 in the compounds of high selenium content including 10%Se-HANs and 2 μM Na_2SeO_3 at different time points of 12, 18, and 24 h (Figure 4A). We found two activated initiators of caspase-9 and caspase-8 in the same compounds of high selenium content (Figure 4B). Moreover, truncated Bid (tBid, 15 KD) derived from original Bid (22 kDa) by the cleavage of caspase-8 was detected in both 10%Se-HANs and 2 μM Na_2SeO_3 (Figure 4B). The generation of tBid further confirmed the initiation of extrinsic apoptotic pathway activated by the apoptotic initiator of caspase-8. Additionally, the tBid was translocated to the mitochondria for stimulating the release of cytochrome c that activated the caspase-9 for starting the intrinsic apoptotic pathway (Figure 4C). Therefore, tBid plays a crucial role in bridging the activation of both extrinsic and intrinsic caspase-dependent apoptotic pathways. Namely, in this study we report a potentially inherent mechanism, a caspases-dependent apoptosis, on tumor impression by selenium.

These findings demonstrate that anti-osteosarcoma activity of Se-HANs is basically manipulated *via* a caspase-dependent apoptosis involving both extrinsic and intrinsic apoptotic pathways. Intracellular ROS generation probably provides an initially synergistic effect on the caspase-dependent apoptosis. On one hand, ROS regeneration likely plays as a vital signal transduction molecule in aggregating the Fas receptor, thereby activating caspase-8 and triggering the death receptor-mediated extrinsic apoptotic pathway.[37–39] On the other hand, ROS can facilitate the permeabilization of mitochondria to release cytochrome c and effectively activate the intrinsic apoptotic pathway.[40] Therefore, our current work not only verifies the key role of ROS generation induced by Se-HANs on tumor apoptosis but also systematically illuminates the inherent mechanism of caspase-dependent apoptosis involving both extrinsic and intrinsic apoptotic pathways.

Se-HANs Induce Apoptosis To Inhibit Tumor Growth while Reducing Systemic Toxicity *in Vivo*

The aforementioned data confirmed that antiosteosarcoma activity of Se-HANs was positively dependent on the selenium content of the compounds, and thus 10%Se-HANs exhibited the better efficacy on inducing tumor apoptosis due to the higher selenium ions content. Here we chose 10%Se-HANs (100 mg/mL) to investigate antineoplastic activity, systemic toxicity, and *in vivo* degradability using a BALB/c nude mouse osteosarcoma model. Based on the calculation of release kinetics, 10%Se-HANs of 100 mg/mL was able

to release approximately 3 mM in the neutral condition (pH 7.4) and 16 mM in the acidic condition (pH 5.0). We thereby designed pure HANs (100 mg/mL) physically mixed with 0, 3, and 16 mM Na_2SeO_3 as controls for *in vivo* evaluation. Our results showed that 10%Se-HANs significantly inhibited tumor growth after treatment for 9 days, and the inhibition capacity was gradually enhanced with the increase of treatment time (Figure S2). After treatment for 30 days, 10%Se-HANs tremendously reduced tumor volume from 5960.76 ± 1910.90 to 1781.57 ± 901.87 mm^3 and tumor weight from 4.84 ± 1.16 to 1.79 ± 0.95 g in comparison with the control (Figure 5A–C). We also found that HANs/Na_2SeO_3 exhibited a selenium dose-dependent tumor inhibition, and HANs/16 mM Na_2SeO_3 presented the least tumor volume and tumor weight among all three controls. Since antitumor activity was mainly dependent on the intratumor selenium concentration, the equivalent selenium content between 10%Se-HANs and HANs/16 mM Na_2SeO_3 showed no significant difference on both tumor volume and tumor weight.

The pathological analysis was further performed by hematoxylin-eosin (HE) staining, immunohistochemical staining of platelet endothelial cell adhesion molecule-1 (CD-31), and terminal deoxynucleotidyl transferase biotin-dUTP nick-end labeling (TUNEL) assay. The results showed that tumor cells with large and oval-shaped nuclei grew well around the abundant blood vessels in the control and pure HANs groups. In contrast, tumors treated with 10%Se-HANs and HANs/16 mM Na_2SeO_3 exhibited the typical apoptotic tumor tissue with poor vascularization and condensed nucleus chromatin (Figure 5D). To determine *in vivo* biodegradability of implanted materials, the residual of these calcium-based biomaterials was identified by von Kossa staining (Figure 5D). We found that there were obvious aggregations of HANs in all control treatments, while the experimental group of 10%Se-HANs was completely degraded. These findings imply that the remarkably antitumor capacity of 10%Se-HANs is highly associated with its efficient biodegradability in acidic environment of the tumor.

Apoptosis of osteosarcoma cells induced by 10%Se-HANs had been confirmed by the brown-stained nucleus in the TUNEL assay (Figure 5D). However, the exact *in vivo* mechanism of such apoptosis was unclear. As we know, the *in vivo* physiological environment is much more complicated than the *in vitro* environment. Hence, cells *in vivo* may have an altered stress response and metabolism compared to *in vitro* model.[30] To determine whether the *in vivo* mechanism of tumor apoptosis induction was consistent with the *in vitro* model, 8 hydroxyguanosine (8-OHdG) and cleaved/activated caspase 3, 8, and 9 were analyzed with immunostaining, respectively. 8-OHdG is a base lesion in DNA due to attack by free radicals, which can be formed under an oxidative stress. Therefore, it has been applied as an indicator for *in vivo* ROS detection.[41] We found that the tumor treated with both 10%Se-HANs and HANs/16 mM Na_2SeO_3 exhibited ROS-induced DNA damage, as the nuclei were positively stained for 8-OHdG (Figure 6A). Furthermore, cleaved caspase 9, 8, and 3 were also positive in 10%Se-HANs as well as the other two selenium-containing groups (Figure 6B–D). These data indicated that the mechanisms of Se-HANs-induced ROS generation and the subsequent caspase-dependent apoptosis involving both extrinsic and intrinsic apoptotic pathways were also adequate for the *in vivo* model.

Despite all mice survived to the experimental end point without showing significant differences on body weight (Figure S3), systemic toxicities varied extremely in different groups based on the analysis of biochemical parameters of blood including aspartate transaminase (AST), blood urea nitrogen (BUN), creatinine (CREA) and lactate dehydrogenase (LDH). *In vivo* systemic toxicity of nude mice should be attributed to two origins. The major one was the waste produced by rapid metabolism of the malignant osteosarcoma cells.[10] Selenium ions could induce apoptosis of osteosarcoma cells, retard tumor metabolism, protect healthy organs from tumor malignancy, and thus reduce the systemic toxicity *in vivo*. The other one was the potential toxicity of overdosed selenium, which may cause a side effect to mice organs and thereby induce a systemic toxicity.[42–44] We found 10%Se-HANs presented the lowest systemic toxicity by profoundly decreasing the levels of AST, BUN, CREA, and LDH compared with the controls, even including the mixture of equal selenium content, HANs/16 mM Na_2SeO_3 (Figure 6E). The possible reason was that gradual selenium release mediated by a pH value from 10%Se-HANs might lead to a high enrichment of selenium at the local tumor with a tiny leakage in normal tissue. The controlled release of selenium enabled Se-HANs to kill the tumor without harming the normal tissue. On the contrary, Na_2SeO_3 mixed with HANs was immediately decomposed after delivery to the targeted tumor and expanded to the adjacent normal tissue. A high dose of Na_2SeO_3 could have an obvious antitumor effect, but also could be dangerous for normal tissue. To determine this inference, we excluded the interference of the tumor malignancy by using a normal BALB/c mouse model to individually investigate the systemic toxicity of the 10%Se-HANs *in vivo*. Our results showed no significant difference in body weight between 10%Se-HANs and the control (saline). However, HANs/16 mM Na_2SeO_3 significantly inhibited ponderal growth after treatment for 18 days (Figure S4). After treatment for 30 days, HANs/16 mM Na_2SeO_3 exerted an evident systemic toxicity by significantly increasing the levels of AST, ALT, and LDH and decreasing the level of ALP, while 10%Se-HANs was nontoxic compared to the other three groups (Figure S5). HANs/16 mM Na_2SeO_3 also increased the visceral index of liver compared to the saline control (Figure S6), which implied the toxicity-induced hepatomegaly. Pathological changes of liver tissue, such as hepatic edema, were further confirmed in mice treated with HANs/16 mM Na_2SeO_3, while 10%Se-HANs showed no obvious histological lesion (Figure S7). These results not only revealed the side effects of selenium over dose in the normal tissues, mainly in the form of the liver toxicity, but also confirmed that 10%Se-HANs could avoid the selenium-caused systemic toxicity by pH-mediated selenium release. Taken together, 10%Se-HANs are more effective in decreasing the systemic toxicity generated from both tumor malignancy and selenium itself than all other controls.

In traditional nanomedicine development for cancer therapy, the drug carriers are usually designed separately from the drug and just a structural excipient without any therapeutic effect.[45] For osteosarcoma treatment, the ideal drug carriers should also fulfill another role as a bone filler. This idea was achieved by doping selenium into the HA lattice to attain the antitumor mineral nanoparticles, Se-HANs. In this study, a caspase-dependent apoptosis induced by Se-HANs was elucidated *in vitro* and *in vivo*, in which both the extrinsic and the intrinsic apoptotic pathways were synergistically activated by ROS generation. Hence, our

work not only proposed a paradigm to design tissue-repairing mineral nanoparticles bearing therapeutic ions for tumor inhibition but also revealed the inherent apoptosis mechanism.

CONCLUSION

In summary, we successfully produced a series of biodegradable and pH-sensitive bone nanoparticles consisting of Se-HANs. *In vitro* cell evaluation demonstrated that Se-HANs had a remarkable antitumor activity and were able to significantly induce the apoptosis of human osteosarcoma cells. Such an antiosteosarcoma capacity exhibited an obvious dose effect, and the higher selenium content of 10%Se-HANs showed an enhanced inhibition effect compared with the controls of HANs with lower selenium content and selenium-free HANs. More importantly, we systematically elucidated the exact mechanism of apoptosis on tumor cells induced by Se-HANs and suggested an inherent caspase-dependent apoptosis pathway synergistically orchestrated with ROS generation. *In vivo* animal evaluation further confirmed that 10%Se-HANs tremendously induced tumor apoptosis, suppressed tumor growth, and reduced systemic toxicity. Consequently, our current findings reveal the mechanism of tumor inhibition by selenium-doped bone mineral nanoparticles.

METHODS

Preparation of Se-HANs

A series of Se-HANs including 3%Se-HANs, 6%Se-HANs, and 10%Se-HANs were separately prepared by a modified method. The molar ratio of selenium and phosphate (Se/P) in the three compounds was 3%, 6%, and 10%, respectively. Briefly, the mixed aqueous solution of $(NH_4)_2HPO_4$ and Na_2SeO_3 was added dropwise to the aqueous solution of $Ca(NO_3)_2{\cdot}4H_2O$ under vigorous stirring at 75 °C, and the pH was adjusted to 10 with the ammonia solution of 25% (v/v). Sodium polyacrylate (PAAS) was used as a dispersant during the deposition reaction. The precipitate was continuously stirred at 75 °C for over 24 h until the generation of a semitransparent and well-dispersed colloid. The specific colloid was further rinsed with the deionized water and collected by centrifugation. We also prepared the control of selenium-free HANs using the same protocol.

Nanoparticles Characterization

XRD (PANalytical B.V., Netherlands) was used to investigate the phase composition of Se-HANs and HANs. Nanoparticle size and zeta potential were examined by DLS (Malvern, U.K.). Morphology and elemental mapping of Se-HANs and HANs were observed by TEM (Tecnai G2 F30, FEI, Holland). To measure the content of selenium ions in Se-HANs, 1 mg of synthesized nanoparticles were fully dissolved in nitric acid and analyzed by inductively coupled plasma mass spectrometry (ICP-MS, ELAN DRC-e, PerkinElmer, U.S.A.).

Release Kinetics of Selenium Ions

The release of selenium ions from Se-HANs was measured using ICP-MS in two different buffer solutions of pH 7.4 and pH 5.0. Briefly, the synthesized nanoparticles were prepared as a suspension solution of 1 mg/mL with a neutral phosphate buffer solution (PBS, pH 7.4) in a 1.5 mL tube. The tubes were subsequently shaken on a water bath shaker at 37 °C. At

each time interval, the tubes were centrifuged, and 1 mL of the supernatant from each tube was collected for ICP-MS analysis. To simulate selenium ion release in lysosome or acidic tumor microenvironment, the PBS was adjusted to pH 5.0, and the experimental procedure was the same as detailed above. Three duplications were prepared for each group. As comparative analysis, we also measured the release of calcium ions from HANs and Se-HANs using QuantiChromTM Calcium Assay Kit (BioAssay Systems, U.S.A.) in the same buffers of pH 7.4 and pH 5.0.

Cellular Uptake and Intracellular Location

Human osteosarcoma cells MNNG/HOS were cultured in MEM medium containing 10% fetal bovine serum, 100 units/mL penicillin, and 100 mg/mL streptomycin, and the medium was changed every 2 days. For TEM observation, Se-HANs were directly added to culture dishes at a concentration of 50 μg/mL and cocultured for 12 h. Cell sections were immediately prepared by following a published protocol[46] and observed with a specific cell TEM (H-7000FA, HITACHI, Japan). For laser confocal scanning microscopy (LCSM) and flow cytometry (FCM) analysis, the synthesized nanoparticles were first labeled with FITC, according to the previously reported method,[47] and sterilized by 75% ethanol. MNNG/HOS cells were placed in 6-well plates with an initial density of 1×10^6 cells/well. The cells were then separately incubated with FITC-labeled Se-HANs and HANs at a concentration of 50 μg/mL for 3, 6, 12, and 24 h. At each time point, the cells were washed with PBS, harvested, and resuspended in PBS. Semiqualitative time course analysis of cellular uptake were measured by intracellular fluorescence intensity using flow cytometry (Cytomics FC500, Beckman Coulter, U.S.A.). For LCSM analysis, MNNG/HOS cells were seeded on sterile glass coverslips in 6-well plates at a density of 2×10^5 cells/well and allowed to attach for 24 h. To each well, 50 μg/mL of FITC-labeled Se-HANs and HANs were added and incubated for 3, 6, 12, and 24 h. LysoTracker Red was then added to stain the lysosome red for 1 h before stopping incubation. At each time point, the cells were washed with PBS, fixed with 4% paraformaldehyde for 20 min, and stained with 10 μg/mL DAPI solution. The intracellular location was visualized under a FluoViewFV1000 CSLM (Olympus, Japan).

Cell Viability

MNNG/HOS cells were seeded at a density of 5×10^3 cells/well in 96-well plates and cultured for 48 h. Both Se-HANs and HANs (50 μg/mL) were added to each well and incubated for 0, 6, 12, 18, 24, 36, and 48 h. Sodium selenite (Na_2SeO_3, 2 μM) was used as a positive control, and pure medium without adding any compounds was designed as a blank control. Cell viability was performed by CCK-8 reagent kit, and the optical density (OD) value was measured by a microplate reader (Eon, BioTek, U.S.A.) at a wavelength of 450 nm.

ROS Generation

ROS generation was measured by intracellular conversion of dichlorofluorescein diacetate (DCFH/DA) into a fluorescent product DCF.[48] MNNG/HOS cells were plated in 6-well plates at a density of 1×10^6 cells/well. After culturing for 16 h, the cells were separately incubated with Se-HANs (50 μg/mL), HANs (50 μg/mL), and sodium selenium (2 μM) for 3, 6, 12, 18, and 24 h. Thereafter, DFCH/DA (1 μM) was added to each well and incubated

at 37 °C for 30 min before cells were detached. The cells were subsequently collected by centrifugation, washed twice with PBS, and resuspended in PBS. ROS generation was measured by the fluorescence intensity (485 nm excitation; 538 nm emission) using a FCM (Cytomics FC500, Beckman Coulter, U.S.A.). To investigate the inhibition effect of ROS generation in the presence of selenium, a ROS depressed model was constructed by adding MnTMPyP (10 μM) to each well to culture for 1 h before incubation with the nanoparticles.

Western Blotting

MNNG/HOS cells were separately treated with Se-HANs (50 μg/mL), HANs (50 μg/mL), and sodium selenite (2 μM) to analyze apoptotic proteins at different designed time points. The cells were lysed on ice for 30 min and centrifuged at 13,000 rpm for 30 min at 4 °C. The supernatant was mixed with the loading buffer, and the protein concentration was determined by the BCA assay. For each group, 30 μg of protein was loaded to SDS-polyacrylamide gel, separated by electrophoresis at 100 V for 2 h, and then transferred to polyvinylidene fluoride (PVDF) membranes. After blocking with TBST (0.1% Tween-20, 10% tri-*sec*-buffer saline, 89.9% deionized water) containing 5% nonfat milk, the membranes were incubated with primary antibodies (all purchased from Cell Signaling) overnight at 4 °C and then incubated with HRP-conjugated secondary antibodies. The immunoreactive blots were observed using the ECL kit (Thermo Scientific Pierce, U.S.A.) with a chemiluminescence system (Bio-Rad).

Immunofluorescence Staining

To investigate the outer mitochondrial permeabilization, a two-color immunofluorescence experiment was performed to detect subcellular localization of cytochrome c. MNNG/HOS cells (1×10^5 cells/well) on glass coverslips were treated with Se-HANs (50 μg/mL), HANs (50 μg/mL), and sodium selenite (2 μM) for 12 h. MitoTracker Red CMXRos was applied at a concentration of 200 nM to stain the mitochondrial for 30 min at 37 °C. The cells were fixed with 4% paraformaldehyde for 20 min at 4 °C, permeablized by 0.3% Triton X-100 for 20 min, and blocked with 1% BSA for 2 h at room temperature. The cells were then incubated with the monoclonal primary antibody (1:300, Cell Signaling) of cytochrome c at 4 °C for overnight. Secondary antibody labeled with Alexa Fluor 488 was added and incubated for 2 h at room temperature. The stained cells were rinsed three times with cold PBS and stained with 10 μg/mL DAPI solution. The morphology of mitochondrial and subcellular localization of cytochrome c were examined using confocal microscopy. (FluoViewFV1000, Olympus, Japan).

Construction of Animal Model

The xenograft osteosarcoma model was constructed using BALB/c nude mice (4–6 weeks) to investigate antitumor activities of Se-HANs *in vivo*. Animal proposal was approved by Institutional Animal Care and Use Committee (IACUC) of Huazhong University of Science and Technology. The osteosarcoma model was inoculated at the left shoulder by injecting 3×10^6 cells/site. Ten days after cell implantation, the tumor volume was approximately 100 mm^3. The mice were randomly divided into 5 groups (6 mice per group) including 10%Se-HANs, HANs/16 mM sodium selenite (high selenium), HANs/3 mM sodium selenite (low

selenium), HANs, and the blank control of physiological saline. The mice were intratumor injected with 20 μL of test nanoparticles for each mouse.

Evaluation of Anti-Osteosarcoma Activity *in Vivo*

The mice were repeatedly treated and weighed every 3 days, and the tumor volume was measured with a vernier caliper according to the equation: volume (mm^3) = (length × $width^2$)/2. On day 30, 500 μL of blood was collected from the tail vein of each mouse, and the blood serum was isolated to analyze some biochemical indicators containing ALT, AST, ALP, BUN, CREA, and LDH. Thereafter, all mice were euthanized, and an autopsy was conducted. The tumors were detached, weighed, and fixed with 10% neutral formalin. Tumor tissues were embedded with paraffin, sectioned at a thickness of 5 μm, and mounted onto slides for histological examination. Tumor growth status and organ tissue lesions were observed using HE staining. *In vivo* degradation of Se-HANs and HANs was analyzed by von Kossa staining by following a standard procedure.[49] Apoptotic osteosarcoma cells in tumor tissues were detected with the TUNEL assay using a cell death detection kit (Roche, Germany). The CD-31, cleaved caspase-8, and cleaved caspase-3 were investigated by immunohistochemical analysis according to a previously reported method.[50] Primary antibodies included anti CD-31 (1:100, R&D) as well as anticleaved caspase-8 and anticleaved caspase-3 (1:100, Cell Signaling). The oxidative damage and caspase-9 activation were detected by immunofluorescence on the paraffin sections of tumors with anti-8-OHdG (1:100, Abcam) and anticleaved caspase-9 (1:50, Santa Cruz), respectively.

Statistical Analysis

One-way analysis of variance (ANOVA) was carried out using SPSS 21.0 with Tukey's multiple comparison tests to determine the significant difference among three or more groups. The level of significance was set as $p < 0.05$, $p < 0.01$, and $p < 0.001$.

Supplementary Material

Refer to Web version on PubMed Central for supplementary material.

Acknowledgments

This work was supported by the Key Project of NSFC (grant no. 31430029) and NSFC (grant nos. 81071263, 81461148032, 81471792, and 30870624), the National Key Technology Research and Development Program of China (grant no. 2012BAI17B02), the National Basic Research Program of China (grant no. 2012CB933601), HUST Key Innovation Team Foundation for Interdisciplinary Promotion (2016JCTD101), and Zhejiang Provincial Natural Science Foundation of China (LZ16E030001). We also thank the Analytical and Testing Center of HUST. J.L.W and C.B.M. would like to thank the financial support from National Institutes of Health (CA200504, CA195607, and EB021339), National Science Foundation (CMMI-1234957), Department of Defense Office of Congressionally Directed Medical Research Programs (W81XWH-15-1-0180), and Oklahoma Center for the Advancement of Science and Technology (HR14-160).

REFERENCES

1. Ward E, DeSantis C, Robbins A, Kohler B, Jemal A. Childhood and Adolescent Cancer Statistics, 2014. Ca-Cancer J. Clin. 2014; 64:83–103. [PubMed: 24488779]
2. Kansara M, Teng MW, Smyth MJ, Thomas DM. Translational Biology of Osteosarcoma. Nat. Rev. Cancer. 2014; 14:722–735. [PubMed: 25319867]

3. Bielack SS, Kempf-Bielack B, Delling G, Exner GU, Flege S, Helmke K, Kotz R, Salzer-Kuntschik M, Werner M, Winkelmann W, Zoubek A, Jurgens H, Winkler K. Prognostic Factors in High-Grade Osteosarcoma of The Extremities or Trunk: An Analysis of 1,702 Patients Treated on Neoadjuvant Cooperative Osteosarcoma Study Group Protocols. J. Clin. Oncol. 2002; 20:776–790. [PubMed: 11821461]
4. Grimer RJ. Surgical Options for Children with Osteosarcoma. Lancet Oncol. 2005; 6:85–92. [PubMed: 15683817]
5. Singal PK, Iliskovic N. Doxorubicin-induced Cardiomyopathy. N. Engl. J. Med. 1998; 339:900–905. [PubMed: 9744975]
6. Sahni V, Choudhury D, Ahmed Z. Chemotherapy-associated Renal Dysfunction. Nat. Rev. Nephrol. 2009; 5:450–462. [PubMed: 19564889]
7. Rybak LP, Ramkumar V. Ototoxicity. Kidney Int. 2007; 72:931–935. [PubMed: 17653135]
8. Rayman MP. Selenium and Human Health. Lancet. 2012; 379:1256–1268. [PubMed: 22381456]
9. Loscalzo J. Keshan Disease, Selenium Deficiency, and the Selenoproteome. N. Engl. J. Med. 2014; 370:1756–1760. [PubMed: 24785212]
10. Wang Y, Hao H, Liu H, Wang Y, Li Y, Yang G, Ma J, Mao C, Zhang S. Selenite-Releasing Bone Mineral Nanoparticles Retard Bone Tumor Growth and Improve Healthy Tissue Functions *In Vivo*. Adv. Healthcare Mater. 2015; 4:1813–1818.
11. Hiraoka K, Komiya S, Hamada T, Zenmyo M, Inoue A. Osteosarcoma Cell Apoptosis Induced by Selenium. J. Orthop. Res. 2001; 19:809–814. [PubMed: 11562125]
12. Yan L. Consumption of a High-Fat Diet Abrogates Inhibitory Effects of Selenium on Spontaneous Metastasis of Lewis Lung Carcinoma in Mice. Carcinogenesis. 2014; 35:2308–2313. [PubMed: 25053624]
13. Harris HR, Bergkvist L, Wolk A. Selenium Intake and Breast Cancer Mortality in a Cohort of Swedish Women. Breast Cancer Res. Treat. 2012; 134:1269–1277. [PubMed: 22736377]
14. Park JS, Ryu JY, Jeon HK, Cho YJ, Park YA, Choi JJ, Lee JW, Kim BG, Bae DS. The Effects of Selenium on Tumor Growth in Epithelial Ovarian Carcinoma. J. Gynecol. Oncol. 2012; 23:190–196. [PubMed: 22808362]
15. Klein EA, Thompson IM, Tangen CM, Crowley JJ, Lucia MS, Goodman PJ, Minasian LM, Ford LG, Parnes HL, Gaziano JM, Karp DD, Lieber MM, Walther PJ, Klotz L, Parsons JK, Chin JL, Darke AK, Lippman SM, Goodman GE, Meyskens FL, et al. Vitamin E and the Risk of Prostate Cancer the Selenium and Vitamin E Cancer Prevention Trial (SELECT). Jama-J. Am. Med. Assoc. 2011; 306:1549–1556.
16. Lippman SM, Klein EA, Goodman PJ, Lucia MS, Thompson IM, Ford LG, Parnes HL, Minasian LM, Gaziano JM, Hartline JA, Parsons JK, Bearden JD, Crawford ED, Goodman GE, Claudio J, Winquist E, Cook ED, Karp DD, Walther P, Lieber MM, et al. Effect of Selenium and Vitamin E on Risk of Prostate Cancer and Other Cancers the Selenium and Vitamin E Cancer Prevention Trial (SELECT). Jama-J. Am. Med. Assoc. 2009; 301:39–51.
17. Dawsey SP, Hollenbeck A, Schatzkin A, Abnet CC. A Prospective Study of Vitamin and Mineral Supplement Use and the Risk of Upper Gastrointestinal Cancers. PLoS One. 2014; 9:e88774. [PubMed: 24558423]
18. Weekley CM, Aitken JB, Vogt S, Finney LA, Paterson DJ, de Jonge MD, Howard DL, Witting PK, Musgrave IF, Harris HH. Metabolism of Selenite in Human Lung Cancer Cells: X-Ray Absorption and Fluorescence Studies. J. Am. Chem. Soc. 2011; 133:18272–18279. [PubMed: 21957893]
19. Shen HM, Yang CF, Ong CN. Sodium Selenite-Induced Oxidative Stress and Apoptosis in Human Hepatoma Hepg(2) Cells. Int. J. Cancer. 1999; 81:820–828. [PubMed: 10328239]
20. Olszta MJ, Cheng XG, Jee SS, Kumar R, Kim YY, Kaufman MJ, Douglas EP, Gower LB. Bone Structure and Formation: A New Perspective. Mater. Sci. Eng., R. 2007; 58:77–116.
21. Yamagishi K, Onuma K, Suzuki T, Okada F, Tagami J, Otsuki M, Senawangse P. Materials chemistry: A Synthetic Enamel for Rapid Tooth Repair. Nature. 2005; 433:819. [PubMed: 15729330]
22. Ma J, Wang YH, Zhou L, Zhang SM. Preparation and Characterization of Selenite Substituted Hydroxyapatite. Mater. Sci. Eng., C. 2013; 33:440–445.

23. Oh N, Park JH. Endocytosis and Exocytosis of Nanoparticles in Mammalian Cells. Int. J. Nanomed. 2014; 9:51–63.
24. Yuan Y, Liu CS, Qjan JC, Wang J, Zhang Y. Size-Mediated Cytotoxicity and Apoptosis of Hydroxyapatite Nanoparticles in Human Hepatoma Hepg2 Cells. Biomaterials. 2010; 31:730–740. [PubMed: 19836072]
25. Roohani-Esfahani SI, Nouri-Khorasani S, Lu Z, Appleyard R, Zreiqat H. The Influence Hydroxyapatite Nanoparticle Shape and Size on the Properties of Biphasic Calcium Phosphate Scaffolds Coated with Hydroxyapatite-PCL Composites. Biomaterials. 2010; 31:5498–5509. [PubMed: 20398935]
26. Zhang XX, Li FF, Guo SY, Chen X, Wang XL, Li J, Gan Y. Biofunctionalized Polymer-Lipid Supported Mesoporous Silica Nanoparticles for Release of Chemotherapeutics in Multidrug Resistant Cancer Cells. Biomaterials. 2014; 35:3650–3665. [PubMed: 24462359]
27. Setyawati MI, Tay CY, Leong DT. Mechanistic Investigation of the Biological Effects of SiO(2), TiO(2), and ZnO Nanoparticles on Intestinal Cells. Small. 2015; 11:3458–3468. [PubMed: 25902938]
28. Giovanni M, Tay CY, Setyawati MI, Xie J, Ong CN, Fan R, Yue J, Zhang L, Leong DT. Toxicity Profiling of Water Contextual Zinc Oxide, Silver, and Titanium Dioxide Nanoparticles in Human Oral and Gastrointestinal Cell Systems. Environ. Toxicol. 2015; 30:1459–1469. [PubMed: 24930694]
29. Song XR, Goswami N, Yang HH, Xie J. Functionalization of Metal Nanoclusters for Biomedical Applications. Analyst. 2016; 141:3126–3140. [PubMed: 27146244]
30. Chia SL, Tay CY, Setyawati MI, Leong DT. Biomimicry 3D gastrointestinal Spheroid Platform for the Assessment of Toxicity and Inflammatory Effects of Zinc Oxide Nanoparticles. Small. 2015; 11:702–712. [PubMed: 25331163]
31. Chia SL, Tay CY, Setyawati MI, Leong DT. Decoupling the Direct and Indirect Biological Effects of ZnO Nanoparticles Using a Communicative Dual Cell-Type Tissue Construct. Small. 2016; 12:647–657. [PubMed: 26670581]
32. Setyawati MI, Tay CY, Leong DT. Effect of Zinc Oxide Nanomaterials-Induced Oxidative Stress on The P53 Pathway. Biomaterials. 2013; 34:10133–10142. [PubMed: 24090840]
33. Ng KW, Khoo SP, Heng BC, Setyawati MI, Tan EC, Zhao X, Xiong S, Fang W, Leong DT, Loo JS. The role Of The Tumor Suppressor P53 Pathway In The Cellular DNA Damage Response To Zinc Oxide Nanoparticles. Biomaterials. 2011; 32:8218–8225. [PubMed: 21807406]
34. Chen XJ, Duan FD, Zhang HH, Xiong Y, Wang J. Sodium Selenite-Induced Apoptosis Mediated by ROS Attack in Human Osteosarcoma U2OS Cells. Biol. Trace Elem. Res. 2012; 145:1–9. [PubMed: 21826611]
35. Luo H, Yang Y, Duan J, Wu P, Jiang Q, Xu C. PTEN-regulated AKT/FoxO3a/Bim signaling contributes to reactive oxygen species-mediated apoptosis in selenite-treated colorectal cancer cells. Cell Death Dis. 2013; 4:e481. [PubMed: 23392169]
36. Vandenabeele P, Galluzzi L, Vanden Berghe T, Kroemer G. Molecular Mechanisms Of Necroptosis: An Ordered Cellular Explosion. Nat. Rev. Mol. Cell Biol. 2010; 11:700–714. [PubMed: 20823910]
37. Huang HL, Fang LW, Lu SP, Chou CK, Luh TY, Lai MZ. DNA-Damaging Reagents Induce Apoptosis Through Reactive Oxygen Species-Dependent Fas Aggregation. Oncogene. 2003; 22:8168–8177. [PubMed: 14603257]
38. Fleury C, Mignotte B, Vayssiere JL. Mitochondrial Reactive Oxygen Species In Cell Death Signaling. Biochimie. 2002; 84:131–141. [PubMed: 12022944]
39. Simon HU, Haj-Yehia A, Levi-Schaffer F. Role of Reactive Oxygen Species (ROS) In Apoptosis Induction. Apoptosis. 2000; 5:415–418. [PubMed: 11256882]
40. Kroemer G, Galluzzi L, Brenner C. Mitochondrial Membrane Permeabilization In Cell Death. Physiol. Rev. 2007; 87:99–163. [PubMed: 17237344]
41. Mugoni V, Postel R, Catanzaro V, De Luca E, Turco E, Digilio G, Silengo L, Murphy MP, Medana C, Stainier DY, Bakkers J, Santoro MM. Ubiad1 is an Antioxidant Enzyme That Regulates eNOS Activity by CoQ10 Synthesis. Cell. 2013; 152:504–518. [PubMed: 23374346]

42. Zhang JS, Wang XF, Xu TW. Elemental Selenium at Nano Size (Nano-Se) as a Potential Chemopreventive Agent with Reduced Risk of Selenium Toxicity: Comparison with Se-Methylselenocysteine in Mice. Toxicol. Sci. 2008; 101:22–31. [PubMed: 17728283]

43. Forceville X, Laviolle B, Annane D, Vitoux D, Bleichner G, Korach JM, Cantais E, Georges H, Soubirou JL, Combes A. Effects of High Doses of Selenium, as Sodium Selenite, in Septic Shock: A Placebo-Controlled, Randomized, Double-Blind, Phase II Study. Crit. Care. 2007; 11:R73. [PubMed: 17617901]

44. Olson OE. Selenium Toxicity in Animals with Emphasis on Man. Int. J. Toxicol. 1986; 5:45–70.

45. Chung JE, Tan S, Gao SJ, Yongvongsoontorn N, Kim SH, Lee JH, Choi HS, Yano H, Zhuo L, Kurisawa M, Ying JY. Self-Assembled Micellar Nanocomplexes Comprising Green Tea Catechin Derivatives and Protein Drugs for Cancer Therapy. Nat. Nanotechnol. 2014; 9:907–912. [PubMed: 25282044]

46. Gratton SEA, Ropp PA, Pohlhaus PD, Luft JC, Madden VJ, Napier ME, DeSimone JM. The Effect of Particle Design on Cellular Internalization Pathways. Proc. Natl. Acad. Sci. U. S. A. 2008; 105:11613–11618. [PubMed: 18697944]

47. Wang JL, Yang GJ, Wang YF, Du YY, Liu HM, Zhu Y, Mao CB, Zhang SM. Chimeric Protein Template-Induced Shape Control of Bone Mineral Nanoparticles and Its Impact on Mesenchymal Stem Cell Fate. Biomacromolecules. 2015; 16:1987–1996. [PubMed: 26079683]

48. Wang H, Joseph JA. Quantifying Cellular Oxidative Stress By Dichlorofluorescein Assay Using Microplate Reader. Free Radical Biol. Med. 1999; 27:612–616. [PubMed: 10490282]

49. Simonet WS, Lacey DL, Dunstan CR, Kelley M, Chang MS, Luthy R, Nguyen HQ, Wooden S, Bennett L, Boone T, Shimamoto G, DeRose M, Elliott R, Colombero A, Tan HL, Trail G, Sullivan J, Davy E, Bucay N, RenshawGegg L, et al. Osteoprotegerin: A Novel Secreted Protein Involved in The Regulation of Bone Density. Cell. 1997; 89:309–319. [PubMed: 9108485]

50. Di Mitri D, Toso A, Chen JJ, Sarti M, Pinton S, Jost TR, D'Antuono R, Montani E, Garcia-Escudero R, Guccini I, Da Silva-Alvarez S, Collado M, Eisenberger M, Zhang Z, Catapano C, Grassi F, Alimonti A. Tumour-Infiltrating Gr-1(+) Myeloid Cells Antagonize Senescence in Cancer. Nature. 2014; 515:134–137. [PubMed: 25156255]

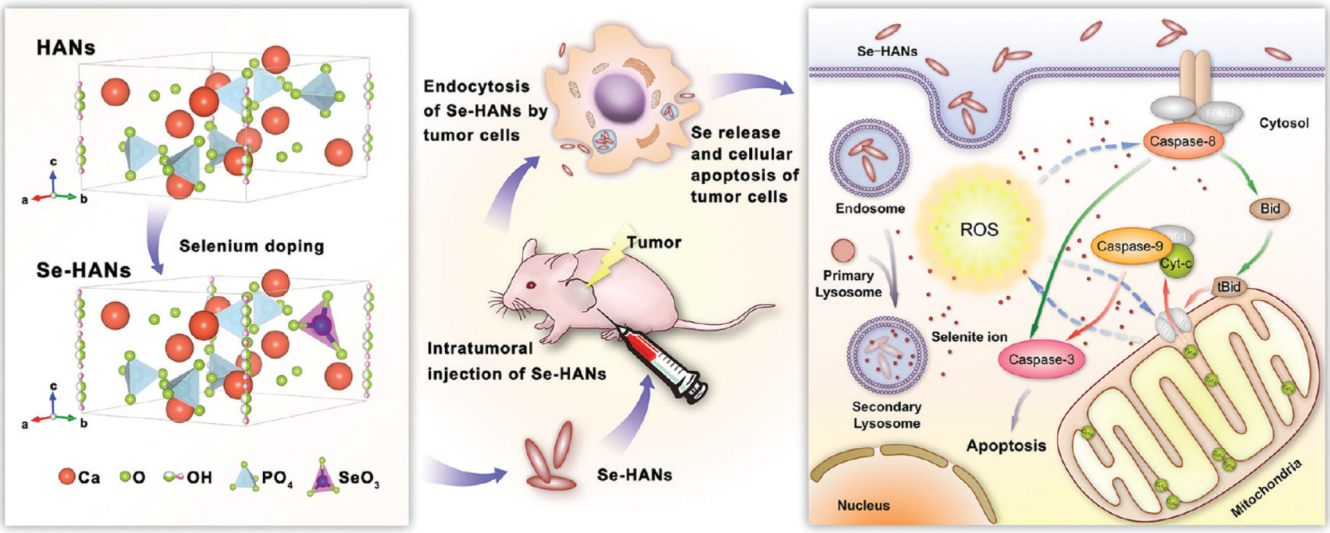

Figure 1.

Preparation and working principle of antitumor nanoparticles. Se-HANs were fabricated using selenite to replace phosphate of HANs. Intratumoral injection of Se-HANs was performed on the xenograft osteosarcoma model. Se-HANs were internalized into tumor cells by nonspecific endocytosis and rapidly degraded in the acidic lysosome to release selenium. Cell apoptosis was activated by a primary, selenium-induced, caspase-dependent apoptosis pathway synergistically orchestrated with the ROS generation.

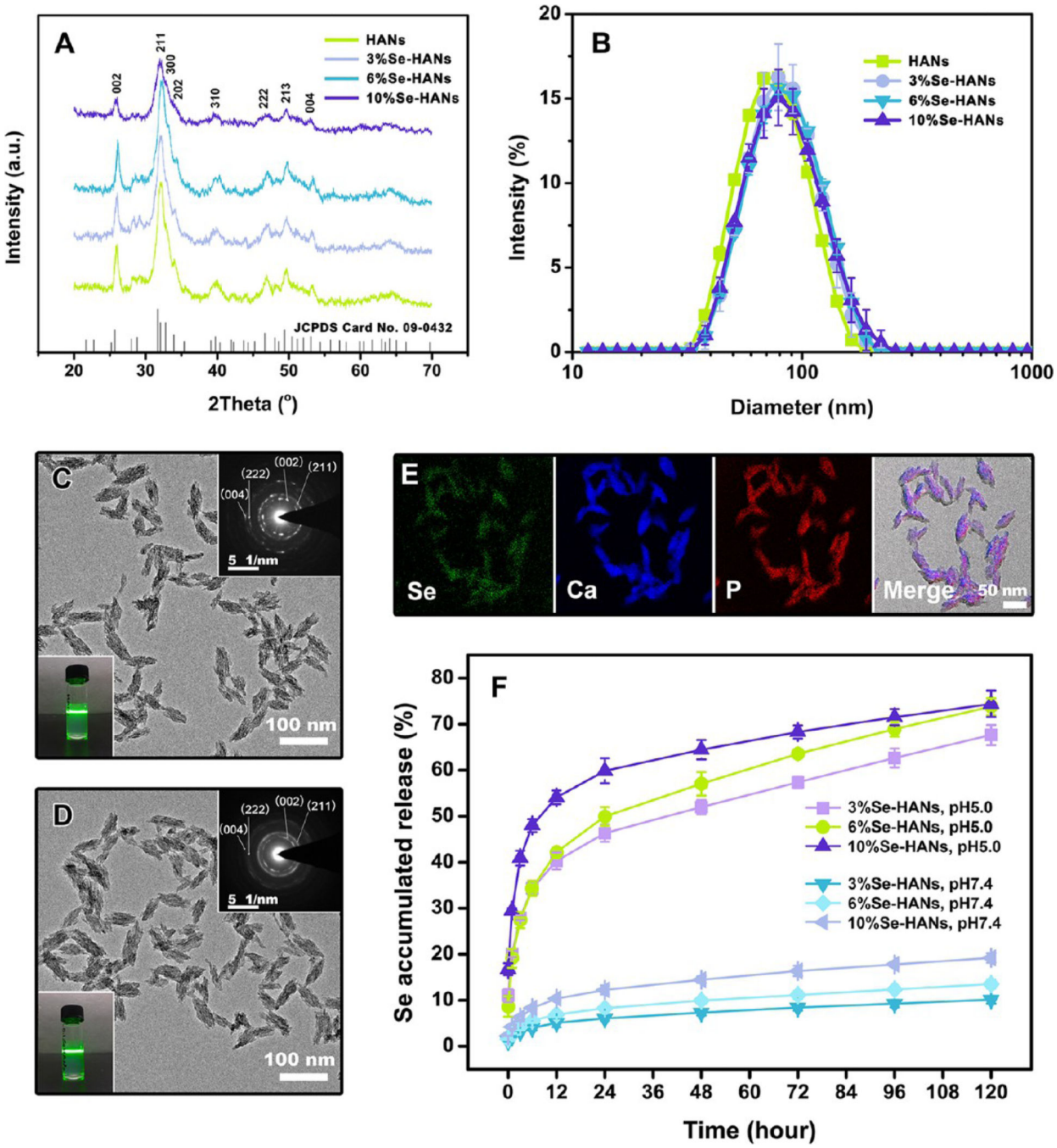

Figure 2.

Nanoparticle characterization and release kinetics of selenium in PBS solutions at pH 5.0 or pH 7.4 (A) XRD patterns confirmed that both Se-HANs and HANs presented the typical peaks of hydroxyapatite (HA), and there was no significant difference between Se-HANs and HANs. (B) DLS indicated both Se-HANs and HANs exhibited very narrow size distributions and centered at around 70 nm. (C, D) TEM images showed nanoparticles of 10%Se-HANs and HANs were needle-like and <100 nm in length. SAED patterns (insets at the top-right corner) indicated that both 10%Se-HANs and HANs were polycrystalline

substances. Tyndall effect (insets at the lower left corner) suggested that both 10%Se-HANs and HANs were capable of forming stable colloid in PBS solution even after setting still for over a month. (E) Analysis of elemental mapping demonstrated that the selenium had a similar elemental distribution as calcium and phosphate in Se-HANs, indicating that the selenium was completely incorporated into the HA lattice and evenly distributed in entire nanoparticles. (F) Selenium release from Se-HANs was much greater in the acidic condition (pH 5.0) than in the neutral condition (pH 7.4), and the accumulated selenium release of 3%Se-HANs, 6%Se-HANs, and 10%Se-HANs in the acidic condition for 12 h was as high as 40.3%, 42.2%, and 54.1%, respectively.

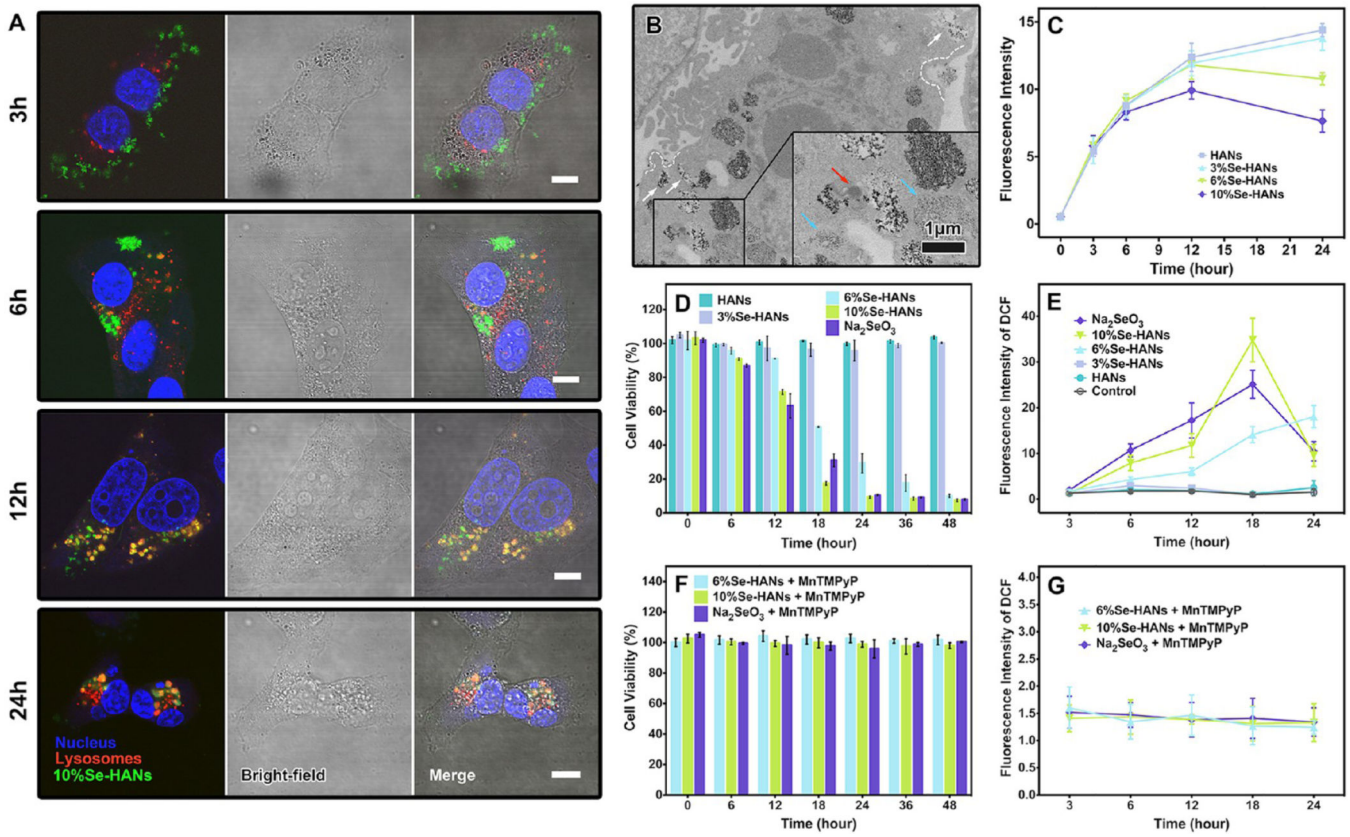

Figure 3.

Intracellular uptake, location, and degradation of nanoparticles to manipulate cell viability and ROS generation. (A) Dynamic uptake and intracellular location of internalized nanoparticles were shown at different time intervals, and more nanoparticles were accumulated with the increase of incubation time. Scale bars are 10 μm. (B) TEM images confirmed that Se-HANs were internalized by human osteosarcoma cells through a typical endocytosis process. White dotted lines delineate cell membrane invagination and endosome formation, white arrows point out newly generated endosomes loaded with nanoparticles, red arrows indicate the primary lysosome combined with the endosome, and blue arrows show the obvious degradation of Se-HANs within the secondary lysosome. (C) Fluorescence intensity of FITC-labeled nanoparticles used as a quantitative indicator of nanoparticle degradation showed that the selenium content in different compounds significantly affected nanoparticle degradation in the lysosome, and the higher selenium ratio generated a faster degradation. (D) Cell viability indicated that a certain amount of selenium was indeed capable of inhibiting the viability of osteosarcoma cells, and the inhibition efficiency was highly positively related to the selenium content. (E) Fluorescence intensity of DCF generated during the process of ROS formation demonstrated that both 3% Se-HANs and HANs exhibited no detectable DCF, whereas there was a remarkable increase of DCF in the compounds with the higher selenium content including 6%Se-HANs, 10%Se-HANs, and 2 μM Na_2SeO_3. (F, G) Under the condition of intracellular ROS generation inhibited by adding MnTMPyP, the compounds with higher selenium content could not result in

detectable DCF and displayed a nearly 100% cell viability without any cell apoptosis throughout the coculture of nanoparticles and cells for 48 h.

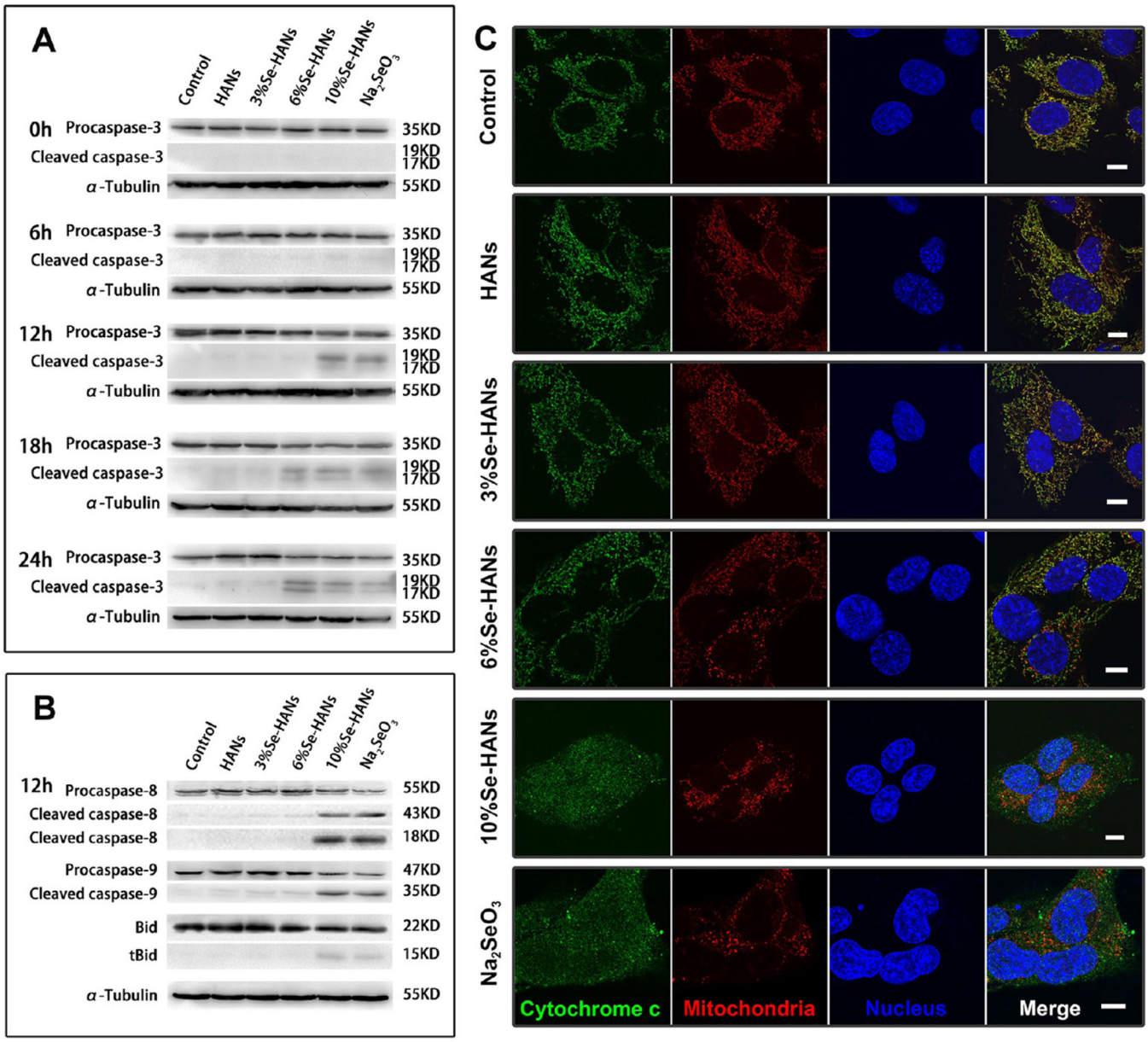

Figure 4.

Caspase-dependent apoptotic pathway. (A) Immunoblotting results indicated that the activated/cleaved caspase-3 was verified at the protein bands of 19 KD and 17 KD in the compounds of high selenium content of 10%Se-HANs and 2 μMNa_2SeO_3 at different time points of 12, 18, and 24 h. (B) Activated/cleaved caspase-9 (35 KD), caspase-8 (43 KD and 18 KD), and tBid (15 KD) as key apoptotic factors were also detected in the same compounds of high selenium content. (C) Release of cytochrome c from the mitochondria into cytosol was detected after coculture of cells and nanoparticles for 12 h. Scale bars are 10 μm.

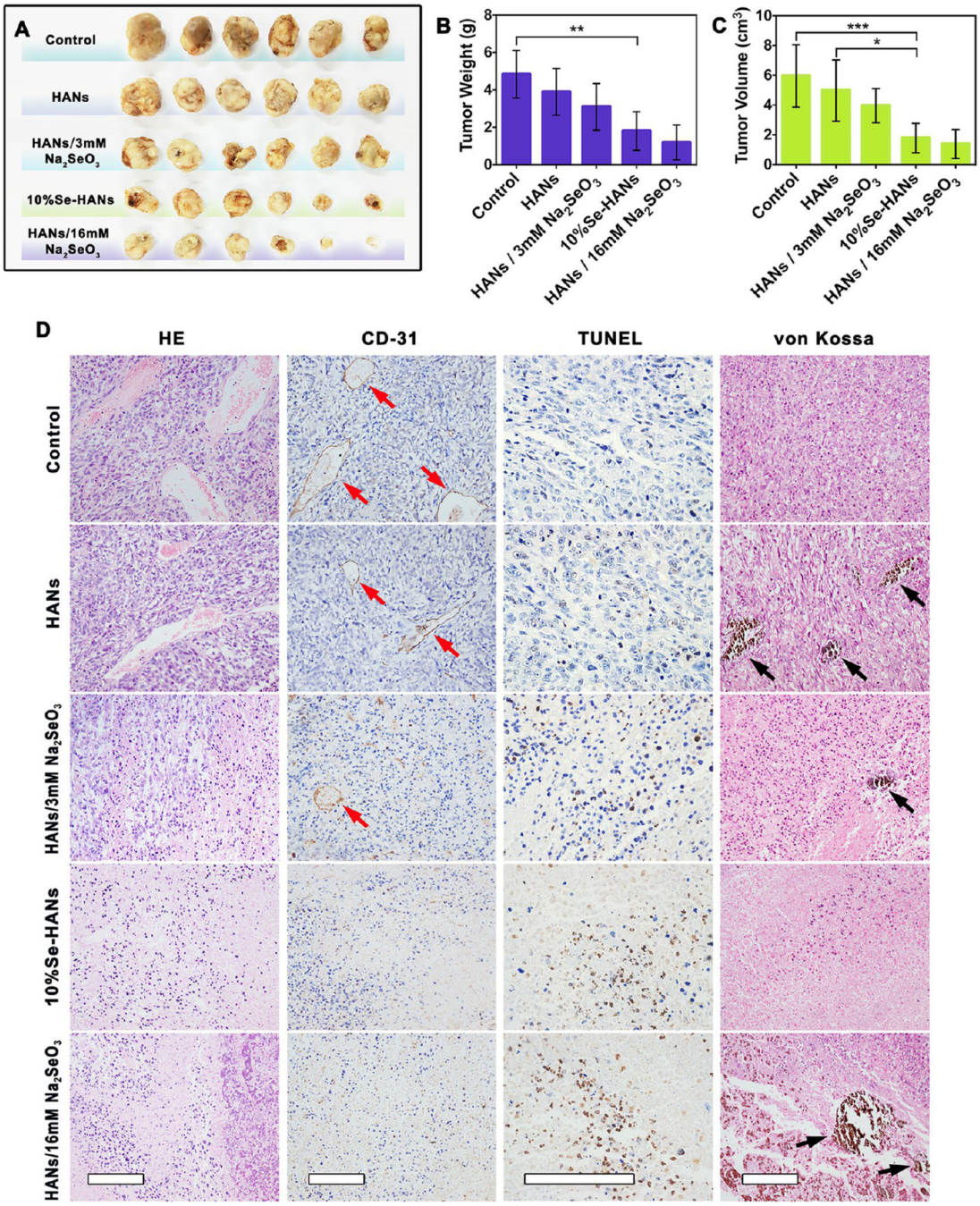

Figure 5.

In vivo evaluation of antiosteosarcoma activity. Compared with pure HANs and HANs/3 mM Na_2SeO_3, the compounds with higher selenium content including 10%Se-HANs and HANs/16 mM Na_2SeO_3 exhibited highly efficient inhibition of tumor growth as evidenced by the reduction of (A) tumor size, (B) tumor weight, and (C) tumor volume (mean ± SD, $n = 6$, $^*p < 0.05$, $^{**}p < 0.01$ and $^{***}p < 0.001$). The pathological analysis further demonstrated that tumors treated with 10%Se-HANs and HANs/16 mM Na_2SeO_3 exhibited the typical apoptotic tumor tissue with poor vascularization and condensed nucleus

chromatin compared with HANs and HANs/3 mM Na_2SeO_3 (D). Calcium staining of von Kossa demonstrated 10%Se-HAN was completely degraded without any obvious calcium aggregations (D). Red arrows show blood vessels within tumor tissue, while black arrows indicate the nondegraded materials that were aggregated to granules in tumor tissue. Scale bars are 100 μm.

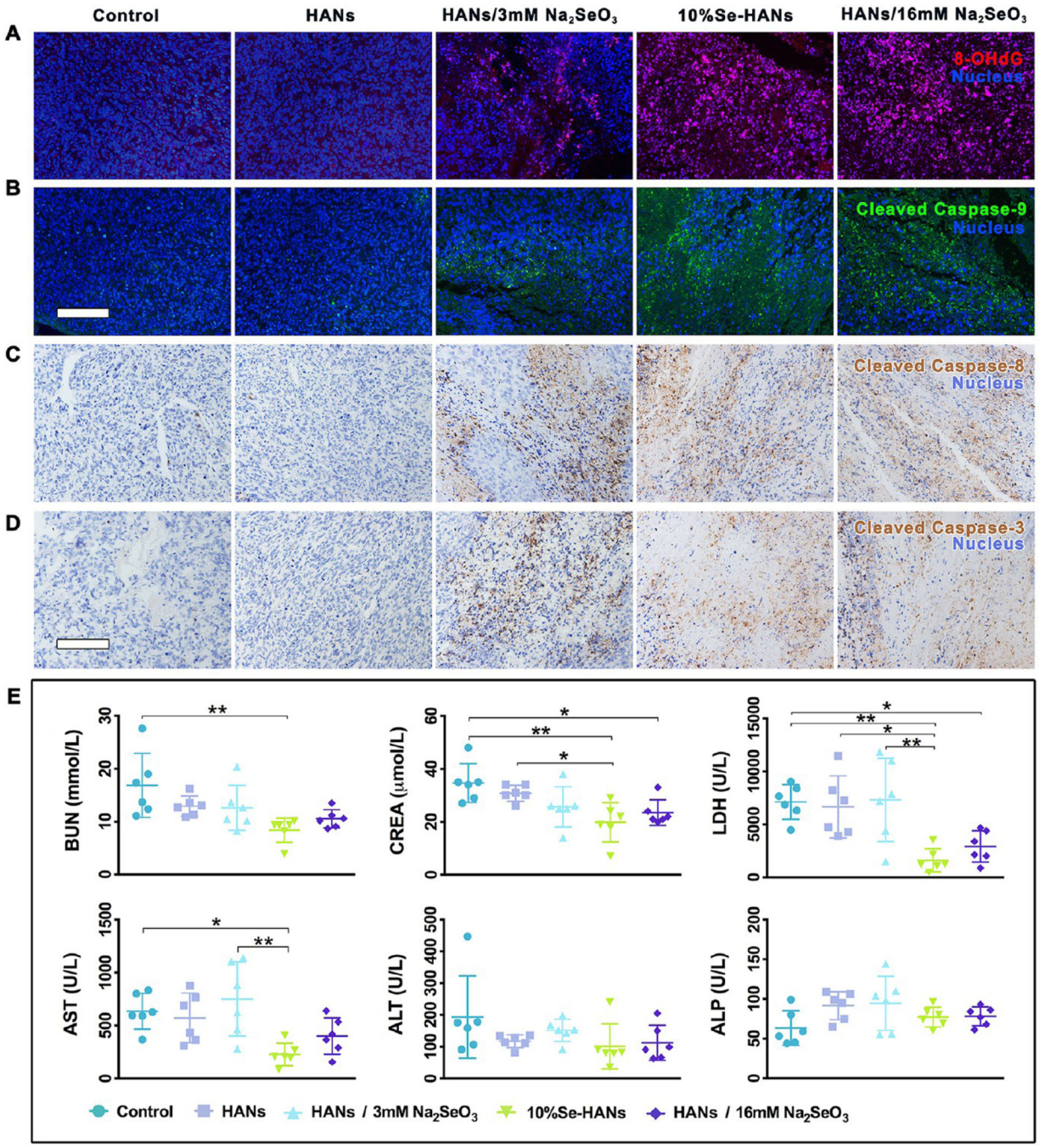

Figure 6.

Se-HANs-induced tumor apoptosis and reduced systemic toxicity *in vivo*. (A) 8-OHdG, (B) cleaved caspase-9, (C) cleaved caspase-8, and (D) cleaved caspase-3 were positive in tumors treated with different selenium contents including 10%Se-HANs, HANs/3 mM Na_2SeO_3, and HANs/16 mM Na_2SeO_3, indicating that the mechanisms of Se-HANs-induced ROS generation and the subsequent caspase-dependent apoptosis were also adequate for the *in vivo* model. Scale bars are 100 μm. (E) Biochemical analysis of blood at the experimental end point showing that 10%Se-HANs exhibited a lowest systemic toxicity by profoundly

declining the levels of AST, BUN, CREA, and LDH compared to the controls. (mean ± SD, $n = 6$, $^{*}p < 0.05$, $^{**}p < 0.01$).